16

Unidirectionally Solidified Eutectic Ceramic Composites for Ultra-High Efficiency Gas Turbine Systems

Yoshiharu Waku
Shimane University
Japan

1. Introduction

To help solve environmental problems, it is vital to develop a material for use in energy conservation technologies and for curbing the emission of pollutants such as CO_2. In the advanced power generation field, studies all over the world are seeking to develop ultra-high temperature structural materials that will improve thermal efficiency in aircraft engines and high-efficiency gas turbines. For example, to improve the thermal efficiency of gas turbines, operating temperatures must be increased and to achieve this, the development of ultra-high temperature resistant structural materials is necessary. Currently Ni-base superalloys are the main thrust in this field, but these have melting points of less than 1673 K, and their strength deteriorates sharply near 1200 K. In order to overcome the high temperature limitations of metals, the development of turbine technology using advanced ceramic matrix composites, has been vigorously pursued in recent years.
It has been reported that a unidirectionally solidified Al_2O_3/YAG eutectic composite has superior flexural strength, thermal stability and creep resistance at high temperature (Mah & Parthasarathy, 1990; Parthasarathy et al., 1990; Parthasarathy et al.,1993) and is a candidate for high-temperature structural materials. However, since the eutectic composite consists of many eutectic colonies, a fairly strong influence of colony boundaries may be predicted (Stubican et al., 1096). The recently developed MGCs are a new class of ceramic matrix composites made by melting and unidirectional solidification of raw material oxides using a eutectic reaction to precisely control the crystal growth. The MGCs have excellent high temperature characteristics due to their unique microstructure without eutectic colony boundaries (Waku et al., 1996; Waku et al., 1997; Waku et al., 2001). In this paper, the fundamental concept of the MGC is explained and compared with sintered polycrystalline monolithic ceramics and single crystal ceramics. High temperature strength, tensile creep properties, compressive deformation, and oxidation resistance and thermal stability as typical high temperature characteristics of the MGCs are introduced. MGC ultra-high efficiency gas turbine systems and the manufacturing process for near-net-shaped MGC component castings are also discussed.

2. Temperature dependence of fracture strength vs microstructure

In general, strength at high temperature depends primarily on the diffusion process, because diffusion-controlled processes dominate at high temperatures and grain boundaries

play a major role in the deformation process (Courtright et al., 1992). The schematic of Fig. 1 illustrates the temperature dependence of fast-fracture strength on microstructure of sintered polycrystalline monolithic ceramics, single crystal ceramics and MGCs. In the case of sintered polycrystalline monolithic ceramics, plastic deformation occurs by micrograin superplasticity due to grain-boundary sliding or rotation at high temperatures, so the fast-fracture strength decreases noticeably with an increase in temperature. Oxide ceramics especially show a sudden drop in fast-fracture strength above 1300 K. In the case of single crystals, diffusion becomes active at high temperatures and there is no barrier (i.e. interface) to disturb the dislocation motion, so the high temperature fast-fracture strength decreases gradually with the increase in temperature.

In contrast to these materials, MGCs have the unique microstructure of a three-dimensionally continuous network of single crystal phases without eutectic colony boundaries. Therefore, MGCs display no grain-boundary sliding or rotation. Additionally, the existence of interfaces in MGCs prevents dislocation motion. Consequently, the MGCs because of their unique microstructure have excellent high temperature fast-fracture strength, superior to the high temperature strength of polycrystalline or single crystal ceramic materials.

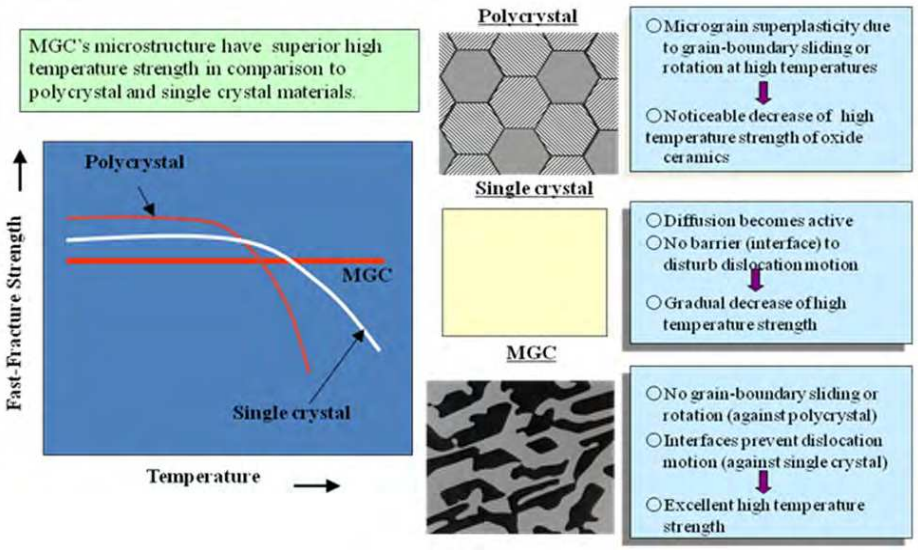

Fig. 1. Schematic illustration of temperature dependence of strength of polycrystal, single crystal and MGC materials.

3. MGC fabrication process

The MGC fabrication process involves unidirectional solidification of eutectic oxide composites as shown in Fig. 2. The preliminary melt was cast into a molybdenum (Mo) crucible (50 mm in outside diameter by 200 mm in length by 5 mm in thickness) placed in a vacuum chamber, and a graphite susceptor was heated by high-frequency induction heating. This heated the Mo crucible and facilitated the melting. After sustaining the melt of

2223 K (about 100 K above melting point) for 30 minutes, the Mo crucible was lowered at 5 mm an hour, completing the unidirectional solidification experiment.
The MGC fabrication process is a unidirectional solidification process that utilizes a eutectic reaction during melting. The MGC forming process is similar to that for single-crystal Ni-based cast superalloys. It is actually performed by lowering of a molybdenum crucible at constant speed using advanced-alloy crystalline-structure-controlling equipment. A detailed experimental procedure has been described in other manuscripts (Waku et al., 1997; Waku et al., 1998).

4. Microstructural characteristics of MGC

4.1 Microtructure

Fig. 3 shows SEM images of the microstructure of a cross-section perpendicular to the solidification direction of Al_2O_3/YAG binary, Al_2O_3/GAP binary and Al_2O_3/YAG/ZrO_2 ternary MGCs. For the Al_2O_3/YAG binary MGC (Fig. 3 (a)), the light area in the SEM microstructure is the YAG phase with a garnet structure, and the dark area is the Al_2O_3 phase with a hexagonal structure (identified by EPMA analysis), the dimensions of the microstructures are 20~30 μm (this dimension is defined as the typical length to the short axis of each domain seen in the cross-section perpendicular to the solidification direction) (Waku et al., 1998).

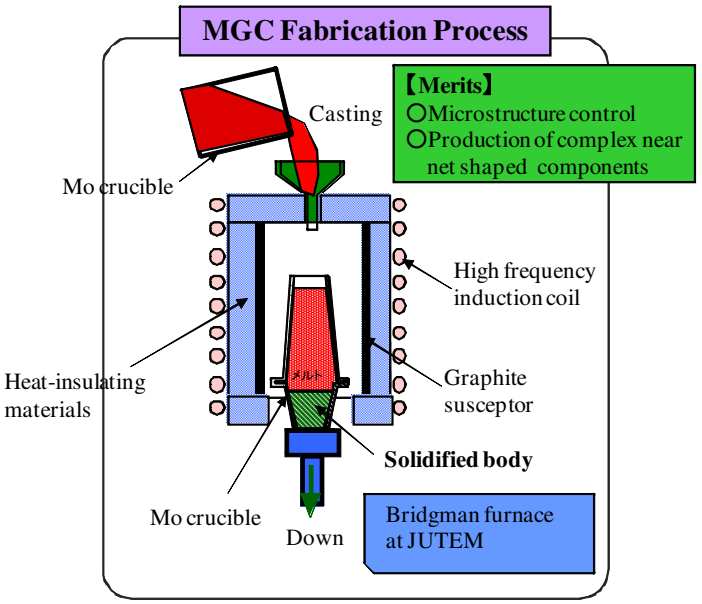

Fig. 2. MGC fabrication process.

For the Al_2O_3/GAP binary system (Fig. 3 (b)), the MGC consists of Al_2O_3 phases with the hexagonal structure and GAP phases with a perovskite structure. In the SEM microstructure, the light area is the GAP phase, the dark area is the Al_2O_3 phase from EPMA analysis. The dimensions of the microstructure of Al_2O_3/GAP binary MGCs are around 3-5

μm smaller than that of around 20-30 μm for the Al_2O_3/YAG binary MGC (Waku et al., 1997).
In the case of the Al_2O_3/YAG/ZrO_2 ternary system (Fig. 3 (c)), the microstructure consists of Al_2O_3, YAG phases and fully stabilized cubic-ZrO_2 phases ($Zr_{0.72}Y_{0.28}O_{1.86}$) with Y_2O_3 (determined from X-ray diffraction patterns). The gray area in the SEM micrograph is the YAG phase, the dark area is the Al_2O_3 phase and light area is the cubic-ZrO_2 (c-ZrO_2) phase (identified by X-ray diffraction and EPMA analysis). The dimensions of YAG phases in the present Al_2O_3/YAG/ZrO_2 ternary MGC are around 2-3 μm smaller in 1/10 than around 20-30μm of the Al_2O_3/YAG binary MGC (Fig. 3 (c)). Many of the c-ZrO_2 phases in the ternary MGC exist at interfaces between Al_2O_3 and YAG phases or in Al_2O_3 phases and seldom exist in YAG phases. Homogeneous microstructures with no pores or colonies are observed in all the binary and ternary MGC (Waku et al., 2001; Waku et al., 2002) .

4.2 Three-dimensional observation of MGC structure

Fig. 4 shows the three-dimensional image of the unidirectionally solidified Al_2O_3/YAG eutectic structure constructed from the reconstructed images (Yasuda et al., 2003). The growth morphology continuously changed, keeping the characteristic feature in the entangled structure. Entangling in the growth direction frequently occurred and the entangled domain was of the same order as the lamellar spacing. The three-dimensional image clearly indicates that the eutectic growth in the Al_2O_3/YAG system was far from the steady state. The specimen used for the CT consisted of α-Al_2O_3 and YAG single crystals, since the X-ray diffractions are consistently identified on the basis of the single crystal crystallographic domain. The following relationship for the crystallographic orientation between the two phases was obtained (Yasuda et al., 2005).

$$(0001)_{Al2O3}//(1\,\bar{1}\,2)_{YAG},[\bar{1}\,100]_{Al2O3}//[1\,\bar{1}\,\bar{1}]_{YAG}$$

This relationship coincides with an earlier work (Frazer et al., 2001). The lamellas tended to align in a certain direction. However, normal vectors of the interface between the Al_2O_3 and the YAG, which were evaluated from the CT images, were scattered over a wide range.
The entangled part in the Al_2O_3/YAG eutectic structure is shown in Fig. 5. A hole observed at the central part indicates that the Al_2O_3 pierces through the YAG. Since time evolution of the eutectic structure remains in the growth direction, the three-dimensional structure lets us know how the entangled part was formed. Branching of the YAG occurred at a position of A in Fig.5 (b). Namely, the Al_2O_3 grew over the YAG. At a position of B, branching of the Al_2O_3 occurred. As a result of the sequential branching of the YAG and the Al_2O_3, the hole in the YAG phase was produced. It should be emphasized that the branching frequently occurs and the entangle domain is of the same order as the lamellar spacing.
It is of interest to compare the branching observed in the Al_2O_3/YAG eutectic structure with that observed in the typical eutectic structures. The micro X-ray CT indicated that branching was rarely observed in regular eutectic structures (Sn-Pb alloys) (Yasuda et al., 2003). In irregular eutectic structures (Sn-Bi alloys), branching of the Bi phase is frequently observed whereas branching of the Sn phase was rarely observed (Yasuda et al., 2003) . The branching of the mate in the eutectic structure did not produce the entangled structure as shown in Fig.5 (b). The sequential branching of both phases results in the entangle structure.

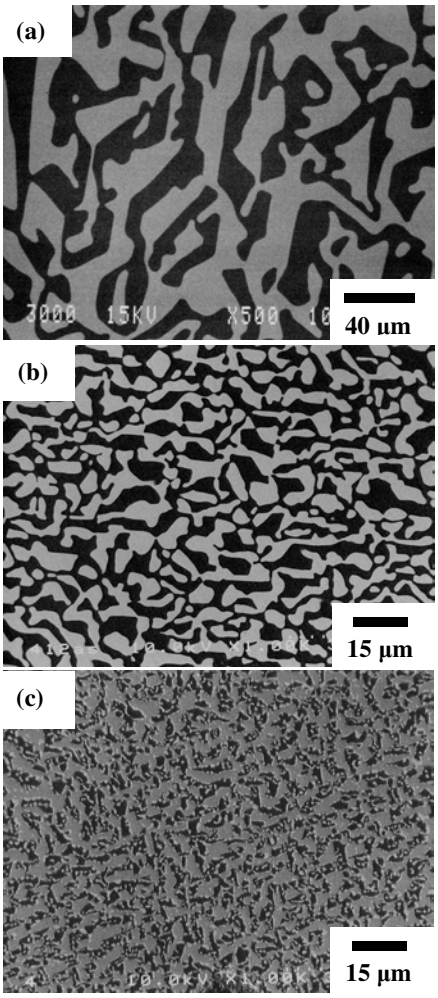

Fig. 3. SEM images showing the microstructure of a cross-section perpendicular to the solidification direction of the MGCs. (a) Al_2O_3/YAG binary system , (b) Al_2O_3/GAP binary system and (c) Al_2O_3/YAG/ZrO_2 ternary system.

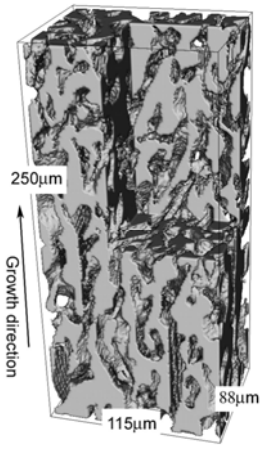

Fig. 4. Three-dimensional image of the unidirectionally solidified Al_2O_3/YAG eutectic structure. The α-Al_2O_3 phase was removed from image.

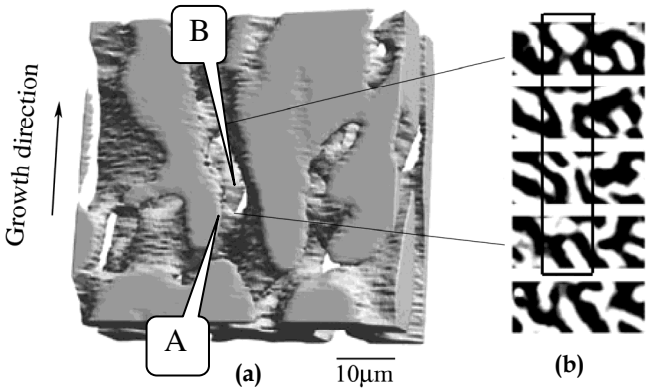

Fig. 5. (a) Three-dimensional image of the YAG phase in the entangled region and (b) sequence of the slice image perpendicular to the growth direction. Black and white phase are YAG and Al_2O_3, respectively.

5. High temperature characteristics of MGCs

5.1 Temperature dependence of flexural strength

The change in flexural strength of the binary and ternary MGCs as a function of temperatures is shown in Fig. 6 compared with those of superalloys (CMSX®-4) (Goulette, 1996), an a-axis sapphire and a Si_3N_4 advanced ceramic (Yoshida, 1998) which was recently developed for high temperature structural materials. Temperature dependence of the flexural strength of these materials is significantly different. With the exception of binary and ternary MGCs, the flexural strength of all other materials falls in a different style with a rise of temperatures. Superalloys are excellent high temperature structural materials in less than about 1300 K, but their strength decreases precipitously at more than about 1300 K. The Si_3N_4 advanced ceramics has the higher flexural strength than that of the other ceramic composite at room temperature, but its strength decreases gradually with an increase of temperatures above approximately 1000 K.

In the case of the a-axis sapphire, the flexural strength is almost the same as that of the Al_2O_3/GAP binary MGC at room temperature, but its strength decreases progressively with increases of temperatures until 1773 K. When the test temperature reaches above 1773 K, flexural strength of the a-axis sapphire drops sharply with rising temperatures.

In contrast, the binary MGCs maintain its room temperature strength up to very high temperature, with a flexural strength in the range of 300~400 MPa for the Al_2O_3/YAG binary MGC(Waku et al., 1996) and 500-600 MPa for the Al_2O_3/GAP binary MGC (Waku et al., 1997). Furthermore, the flexural strength of the Al_2O_3/YAG/ZrO_2 ternary MGC increases gradually with a rise in temperatures and its average flexural strength at 1873 K shows approximately 800 MPa, more than twice 350 MPa of the Al_2O_3/YAG binary MGC (Waku et al., 2002). This difference of the flexural strength's temperature dependence between binary and ternary MGCs is presumed to depend mainly on the dimensions of microstructure. Therefore, the higher high-temperature strength increases, the finer dimensions of microstructure become.

5.2 Tensile deformation

Fig.7 shows the nominal tensile stress-elongation curve obtained from tensile tests of an Al_2O_3/YAG binary MGC from room temperature to 2023 K. Above 1923 K a yield phenomenon occurs and the composites fracture after around 10-17%plastic deformation. The yield stress is about 200 MPa at 1923 K. Several cracks appeared in the microstructure at both the 1650 and 2023 K temperature levels. Nearly all of the cracks were in the YAG phase,with almost none observed in the Al_2O_3 phase. A SEM observation of the fracture surface at tensile testing reveals a constricted area in which a ductile fracture can be observed in the Al_2O_3 phase. In a part of the image, dimple-shaped fracture surface can also be observed. Also,the type of fracture is mixed; intergranular and transgranular fracture are both present.

Fig. 8 shows bright field TEM images of dislocation structures observed in the plastically deformed specimen in the tensile test at 1973 K for the Al_2O_3/YAG single crystal composite. Though the dislocation structures are to be observed in both single crystal Al_2O_3 and single crystal YAG, showing that the plastic deformation occurred by dislocation motion, dislocation densities and dislocation structures in both phases are largely different. Namely, many linear dislocations are observed in single crystal Al_2O_3. Meanwhile, low dislocationdensity is observed in single crystal YAG (Waku et al., 1998).

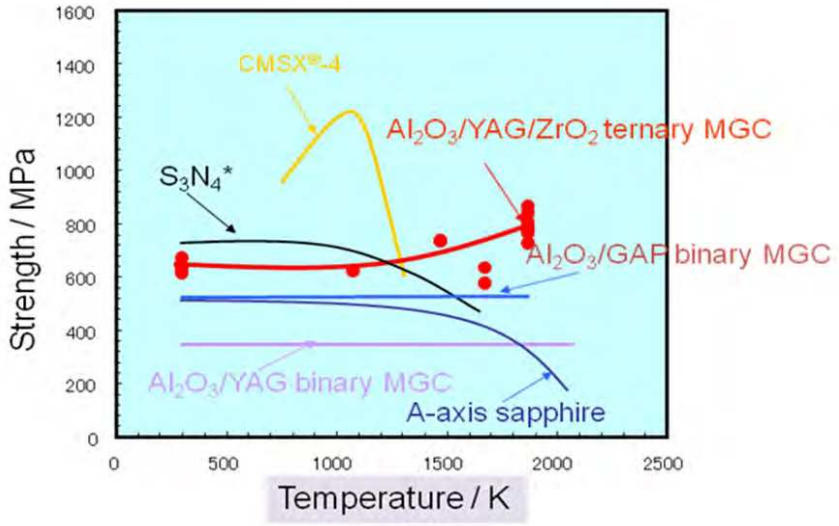

Fig. 6. Temperature dependence of flexural strength of the Al_2O_3/YAG, Al_2O_3/GAP binary and the Al_2O_3/YAG/ZrO_2 ternary MGCs in comparison with superalloys (CMSX-4), an a-axis sapphire and a Si_3N_4 sintered advanced ceramic.

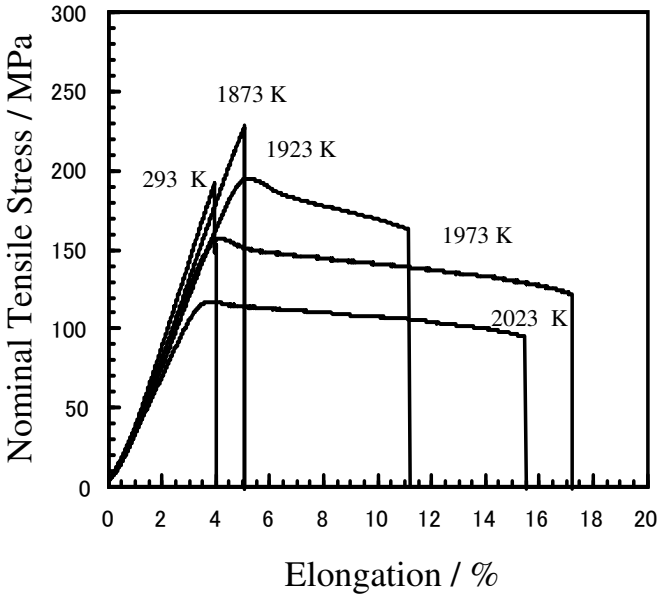

Fig. 7. Nominal tensile stress – elongation curves of an Al_2O_3/YAG single crystal composite from room temperature to 2023 K.

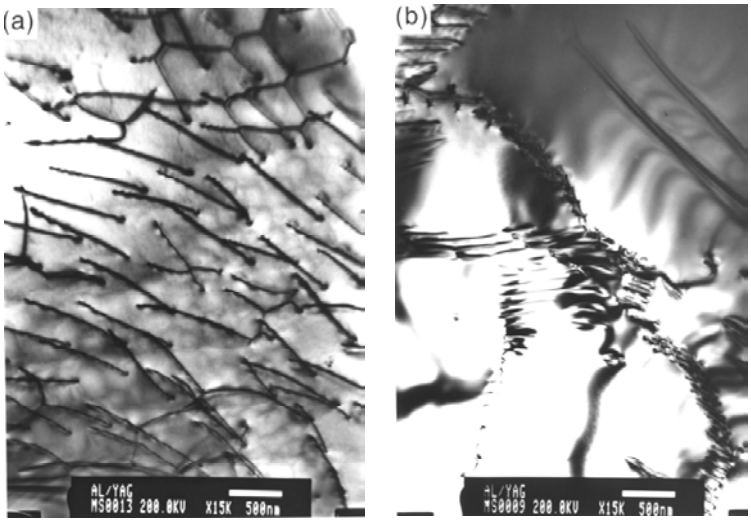

Fig. 8. TEM images showing the dislocation structures of (a) Al_2O_3 phases and (b) YAG phases of the plastically deformed specimens after the tensile test at 1973 K of the Al_2O_3/YAG single crystal composite.

5.3 Compressive deformation

Fig. 9 shows the relationship between compressive flow stress and the strain rate in an Al_2O_3/YAG single crystal composite and a sintered composite at test temperatures of 1773, 1873 and 1973 K. While the Al_2O_3/YAG single crystal composite and the sintered composite shared the same chemical composition and constitutional phases, their compressive deformation was markedly different. That is, the same strain rate of 10-4/s and test Al_2O_3/YAG single crystal composite's flow stress was approximately 13 times higher at 433 MPa. Moreover, as can be seen from the diagram, the Al_2O_3/YAG single crystal composite has creep characteristics that surpass those of a-axis sapphire and, as a bulk material, displays excellent creep resistance (Waku & Sakuma, 2000).

Fig. 10 shows the bright field TEM images of dislocation structure observed in the specimen plastically deformed around l4% in the compressive test at an initial strain rate of 10^{-5}/s and test temperature of 1873 K for an Al_2O_3/YAG single crystal composite and a sintered composite. Dislocation structure is observed in both Al_2O_3 phase and YAG phase for the Al_2O_3/YAG single crystal composite, showing that the plastic deformation occurred by dislocation motion (Wake & Sakuma, 2000; Waku et al., 2002). While dislocation was not observed in both Al_2O_3 phase and YAG phase for the sintered composite. The dislocation structures observed in the Al_2O_3/YAG single crystal composite also indicate that the plastic deformation mechanism of the present eutectic composite is essentially different from that of the sintered composite similar to the micrograin superplasticity of ceramics due to a grain-boundary sliding or a liquid phase present at grain boundary at a high temperature.

The steady state creep rate $\dot{\varepsilon}$ can be usually shown by the following equation:

$$\dot{\varepsilon} = A\sigma^{n}\exp(-Q/RT)$$

Here, A and n are dimensionless coefficients, σ is the creep stress, Q is the activation energy for the creep, T is the absolute temperature, while R is the gas constant.

In Fig. 9,the value of n is around 1-2 for sintered composites, and 5－6 for Al_2O_3/YAG single crystal composites. In sintered composites, it can be assumed that the creep deformation mechanism follows the Nabarro-Herring or Coble creep models,while in Al_2O_3/YAG single crystal composites,the creep deformation mechanism can be assumed to follow the dislocation creep models corresponding to the dislocation structure in Fig. 10. The activation energy Q is estimated to be about 700 kJ/mol from an Arrhenius plot, which is not so different from the values estimated from the high temperature creep in Al_2O_3 single crystal (compression axis is [110]) and YAG single crystal (compression axis is [110]). It is also reported that the activation energy for oxygen diffusion in Al_2O_3 is about 665 kJ/mol, which is not so far from the activation energy of Al_2O_3 single crystal for plastic flow even though that of A^+ diffusion is about 476 kJ/mol. This fact means that the deformation mechanism of the Al_2O_3 single crystal is the diffusion controlled dislocation creep. On the other hand,the activation energy for oxygen diffusion in YAG is about 310 kJ/mol, which differs significantly from the activation energy of YAG single crystal for plastic now. However,dislocation is always observed in both Al_2O_3 phase and YAG phase of compressively deformed specimens at 1773 K-1973 K and at strain rate of 10^{-4}/s – 10^{-6}/s. Therefore,the compressive deformation mechanism of the Al_2O_3/YAG single crystal composite must follow the dislocation creep models (Wake & Sakuma, 2000; Waku et al., 2002).

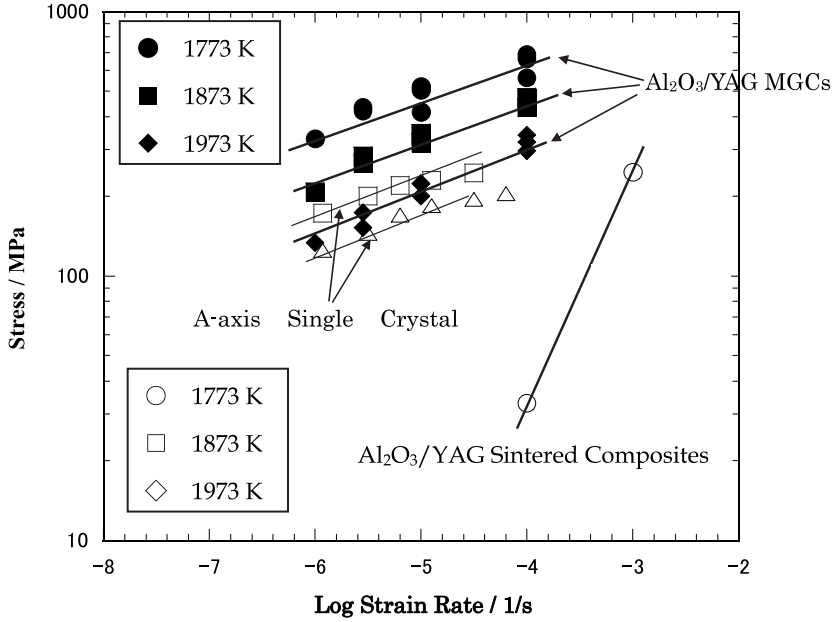

Fig. 9. Relationship between compressive flow stress and strain rate for an Al_2O_3/YAG single crystal composite, a sintered composite and an a-axis sapphire.

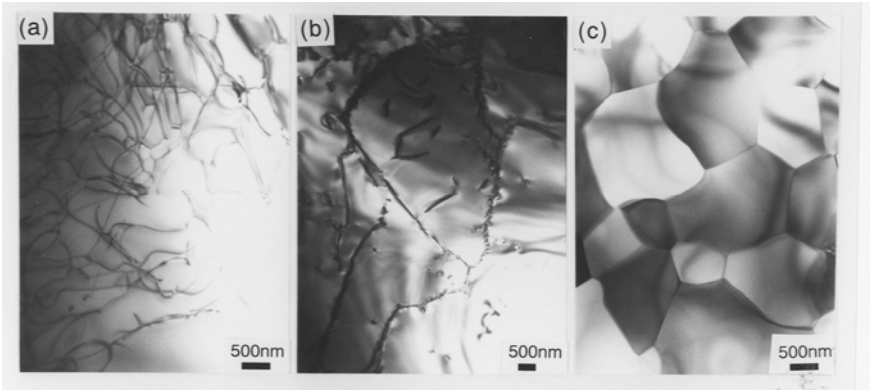

Fig. 10. TEM images showing the dislocation structure of (a) Al_2O_3 phases and (b) YAG phases in the Al_2O_3/YAG single crystal composite, and (c) the microstructure of Al_2O_3 and YAG phases in the sintered composite, of compressively crept specimens at 1873 K and strain rate of 10^{-5}/s.

5.4 Tensile creep rupture

To date a lot of isolated studies have been done on the creep behavior of various highly resistant structural materials. A direct comparison of creep results from different sources is not simple because they have usually been obtained under different test conditions; for instance, with different combinations of temperature and stress. To make a meaningful comparison of creep resistance, the creep data was evaluated here using a Larson-Miller parameter. Figure 3 shows the relationship between tensile creep rupture strength and Larson-Miller parameter, T(22+log t) (DiCarlo & Ynn 1999), for Al_2O_3/YAG binary MGC compared with that of polymer-derived stoichiometric SiC fibers: Hi-Nicalon Type S (Yun & DiCarlo, 1999), Tyranno SA (1, 2) (Yun & DiCarlo, 1999), and Sylramic (1) (Yun & DiCarlo, 1999) , those of silicon nitrides (Krause, 1999), an Al_2O_3/SiC nanocomposite (Ohji, 1994).
Here T is the absolute temperature; t is the rupture time in hours. For comparison, the Larson-Miller curve for a representative superalloy, CMSX®-10 (Erickson, 1996), is shown in Fig. 11 as well.
The relationship between tensile creep rupture strength and Larson-Miller parameter shows three broad regions. The Larson-Miller parameter for CMSX® -10 is 32 or less in region I. This material is already being used for turbine blades in advanced gas turbine systems at above 80% of its melting temperature, and its maximum operating temperature is approximately 1273- 1373 K. It is not envisioned that the heat resistance of this superalloy will be significantly improved in the future. On the other hand, advanced ceramics such as silicon nitrides, SiC fibers, and a nanocomposite are found in region II where the Larson-Miller parameter is between 33 and 42. These materials are promising candidates for high temperature structural materials. They have better high temperature resistance than the superalloys. The creep strength of SiC fibers is approximately coincident with that of silicon nitrides and significantly higher than that of the Al_2O_3/SiC nanocomposite.
In contrast, the Al_2O_3/YAG binary MGC is found in region III where the Larson-Miller parameter is between 44 and 48. The high temperature resistance of this MGC is superior to that of the silicon nitrides, the SiC fibers and the Al_2O_3/SiC nanocomposite. The creep

deformation mechanisms for the MGC are believed to be essentially different from the grain boundary sliding or rotation of the sintered ceramics. We conclude that the network microstructure of MGC can be regarded as a suitable microstructure for super high temperature material (Waku et al., 2004).

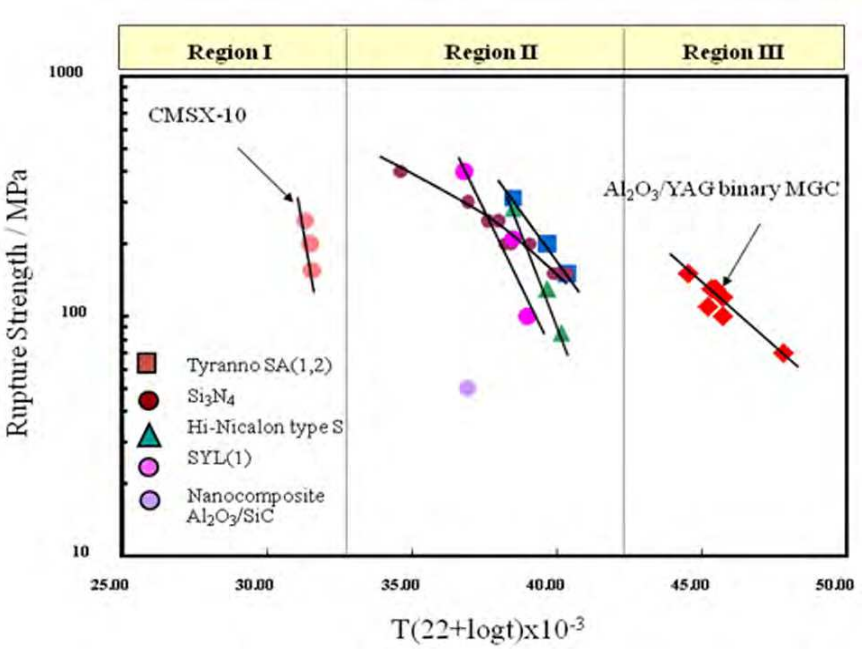

Fig. 11. Larson-Miller creep rupture strength of MGC compared to other heat-resistant materials.

5.5 Oxidation resistance and thermal stability

Fig. 12 shows the change in mass of eutectic composites manufactured by the unidirectional solidification method when these eutectic composites are exposed for a fixed period in an air atmosphere at 1973 K. For a comparison, Fig. 12 also shows the results of oxidation resistance tests performed under the same conditions on ceramics SiC and Si_3N_4. As the Fig. 12 shows, Si_3N_4 was shown to be unstable. When it was exposed to 1973 K for 10 hours in the atmosphere, the following reaction took place; $Si_3N_4 + 3O_2 \rightarrow 3SiO_2 + 2N_2$ and the collapse of the shape of the Si_3N_4 occurred. Likewise, when SiC was held at 1973 K for 50 hours, it was also shown to be unstable. The following reaction took place; $2SiC + 3O_2 \rightarrow 2SiO_2 + 2CO$ and the collapse of the shape also occurred (Waku et al., 1998).

On the other hand, when the unidirectionally solidified Al_2O_3/YAG eutectic composite was exposed in an air atmosphere at 1973 K for 1000 hours, the composite displayed excellent oxidation resistance with no change in mass whatsoever (Waku et al., 1998).

Fig. 13 shows the relationship between flexural strength and heat treatment time at 1973 K in an air atmosphere. For comparison, Fig. 13 also shows results for SiC and Si_3N_4. When the unidirectionally solidified eutectic composite was tested following exposure, there were no

changes in flexural strengths both at room temperature and 1973 K, demonstrating that the composite is an extremely stable material. In contrast, when SiC and Si_3N_4 were heated to 1973 K in an air atmosphere for only 15 minutes, a marked drop in flexural strength occurred. Figure 9 shows changes in the surface microstructure of these test specimens before and after heat treatment. There was little difference in surface microstructure of the unidirectionally solidified eutectic composite following 1000 hours of oxidation resistance testing (Waku et al., 1998).

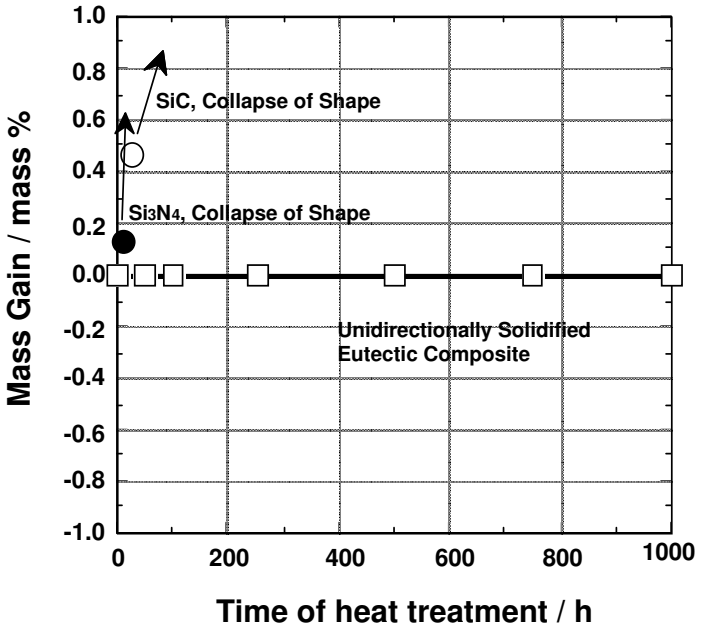

Fig. 12. Comparison of oxidation resistance characteristics of a unidirectionally solidified eutectic composites and advanced ceramics SiC and Si_3N_4 at 1973 K in an air atmosphere.

Al_2O_3/YAG and Al_2O_3/EAG binary MGCs have excellent oxidation resistance with no change in mass gain for 1000 hours at 1973 K in an air atmosphere(Waku et al., 1998). There were also no changes in flexural strength both at room temperature and 1973 K even after heat treatment for 1000 hours at 1973 K in an air atmosphere. In contrast, when advanced ceramic Si_3N_4 was exposed to 1973 K for 10 hours in the atmosphere, the collapse of the shape occurred. Likewise, when SiC was held at 1973 K for 50 hours, it was also shown to be unstable owing to the collapse of the shape also occurred.

Fig. 14 shows SEM images of the microstructure of an Al_2O_3/EAG binary MGC after 500 750, 1000 hours of the heat treatment at 1973 K in an air atmosphere. Even after 1000 hours of heat treatment no grain growth of microstructure was observed. The MGCs were shown to be very stable during lengthy exposure at high temperature of 1973 K in an air atmosphere. This stability resulted from the thermodynamic stability at that temperature of the constituent phases of the single-crystal like Al_2O_3 and the single-crystal EAG, and the thermodynamic stability of the interface. In contrast, a sintered composite shows grain

growth and there are many pores lead to reduction of strength at 1973 K only for 100hr (Nakagawa et al., 1997; Waku et al., 1998).

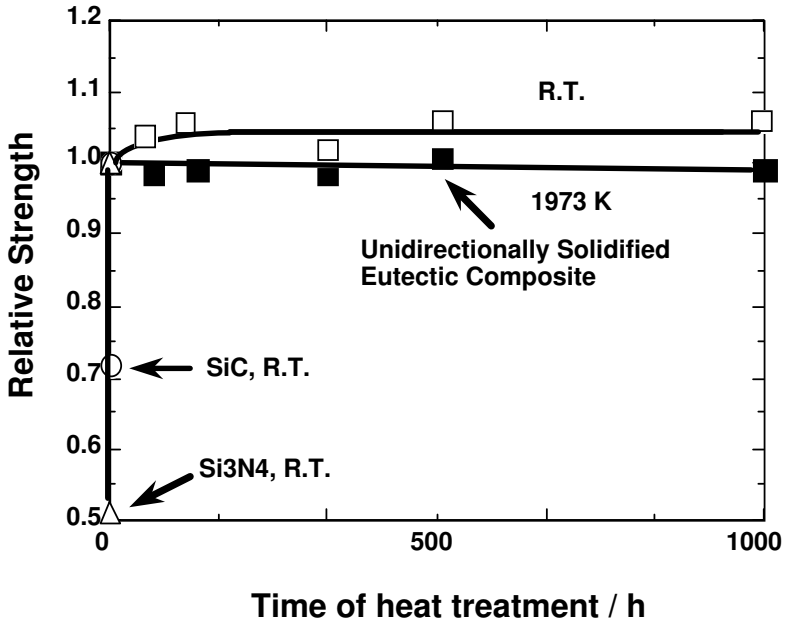

Fig. 13. Changes caused by length of heating in relative strength of unidirectionally solidified eutectic composites and advanced ceramics SiC and Si_3N_4 at room temperature at 1973 K. The relative strength is the ratio of flexural strength after a prescribed period of heating in an air atmosphere at 1973 K to as-received flexural strength.

6. MGC gas turbine systems

Feasibility studies were performed for a leading research project during 1988-2000 in Japan. Based on the results, work was conducted under a NEDO national project from 2001 to 2005. The objective of this project is the development of a 1973 K class uncooled, TBC/EBC-free gas turbine system using MGCs. A paper engine was designed to study component requirements and to estimate its performance. The size of the gas turbine chosen was a relatively small 5MW class. By increasing TIT from the conventional 1373 K to 1973 K, without cooling the nozzle vane and raising the engine pressure ratio from 15 to 30, the thermal efficiency of the gas turbine increased from 29% to 38%. Fig. 15 shows the estimated improvement compared with a current gas turbine. Both are simple cycle gas turbines, and the efficiency is defined at the electrical output (Kobayashi, K., 2002). The final targets of the national project for the MGC gas turbine system are: output power: 5MW class, overall

pressure ratio: 30, turbine inlet temperature (TIT): 1973 K, and a non-cooled MGC turbine nozzle. The relationship between the thermal efficiency and the specific power depends strongly on the turbine inlet temperature and the overall pressure ratio. The current efficiency of a 5MW-class gas turbine is around 29%. In contrast, the efficiency of the MGC gas turbine with the uncooled turbine nozzle is higher than that of the conventional gas turbine. For a TIT of 1973 K and a pressure ratio of 30, the 29% efficiency of the conventional 5 MW-class gas turbine increases to 38%.

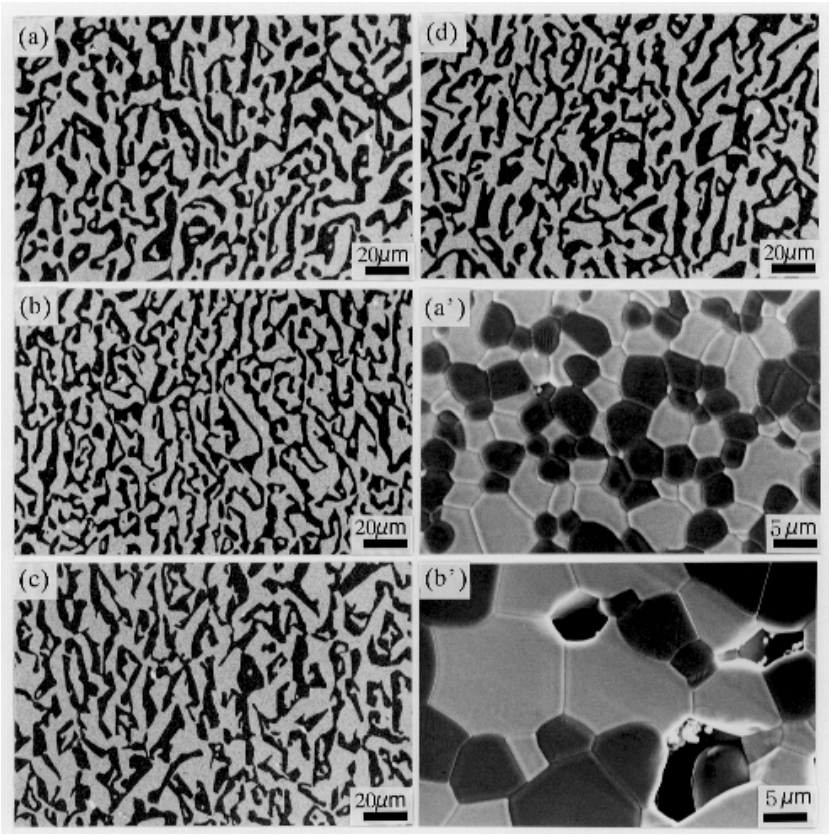

Fig. 14. SEM images showing thermal stability of the microstructures at 1973 K in an air atmosphere in Al_2O_3/EAG binary MGCs: (a) as-received, after heat treatment for (b) 500 h, (c) 750 h, (d) 1000 h and Al_2O_3/EAG sintered composites: (e) as-received and after heat treatment for (f) 100 h.

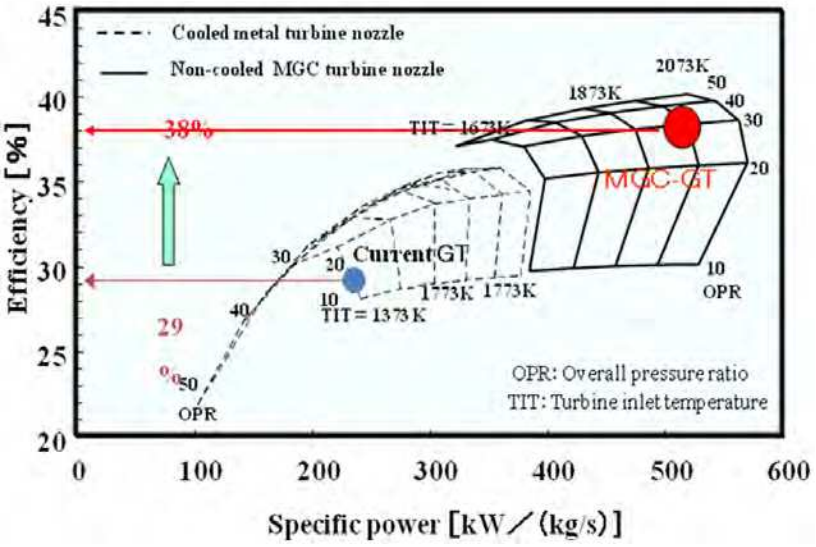

Fig. 15. Gas turbine performance curve as a function of specific power.

MGCs have outstanding high temperature characteristics up to a very high temperature, but the MGC has low thermal shock resistance. First, a hollow nozzle vane was tested at the maximum temperature of 1673 K which is the maximum allowable temperature for the current nozzle rig. The estimated maximum steady state stress using the measured temperature distribution was 211 MPa. To decrease the steady state stress more, a bowed stacking nozzle design is being developed.

An Al_2O_3/GAP binary MGC with high temperature strength superior to that of an Al_2O_3/YAG binary is being examined as a candidate material for the bowed stacking nozzle. Fig. 16 shows the external appearance of the bowed stacking nozzle machined from an Al_2O_3/GAP binary MGC ingot, 53 mm in diameter and 700 mm in length. The steady state temperature and thermal stress distribution at a TIT of 1973 K (see Fig 17) have been analyzed. The maximum temperature is around 1973 K, and it is observed along the central vane section from leading edge to trailing edge at the surface of the bowed stacking nozzle. The maximum steady state thermal stress, generated at the trailing edge of the nozzle, is estimated at 117 MPa. On the other hand, the maximum transient tensile stress in the bowed stacking nozzle during shut-down in one second from 1973 K to 973 K, generated at the leading edge near the mid-span location at 1373 K-1473 K, is estimated at 482 MPa (see Fig. 18). This value is smaller than the estimated ultimate flexural strength of 770 MPa at 1773K of the Al_2O_3/GAP binary MGC (Waku et al., 2003). A rig test at a gas inlet temperature of 1973 K is planned in order to ensure the structural integrity under steady state and thermal shock conditions. The bowed stacking nozzle in Fig. 16 was manufactured from an Al_2O_3/GAP binary MGC ingot by machining with a diamond wheel. Existing rig equipment is being improved for the 1973 K test to enable measurement of a continuous temperature distribution on the nozzle surface by using an infrared camera. It is feasible to verify the structural integrity of the MGC bowed stacking turbine nozzle using this equipment under these hot gas conditions.

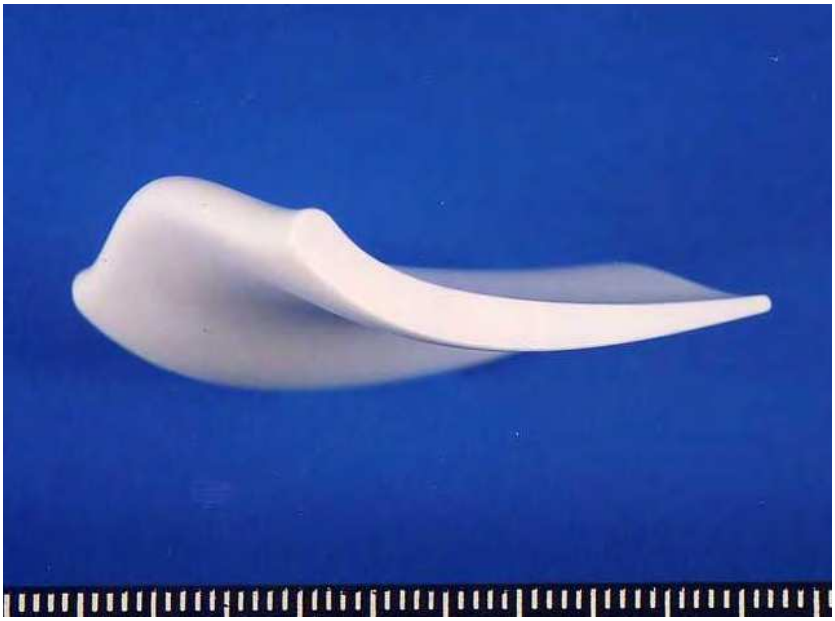

Fig. 16. A bowed stacking nozzle manufactured from an Al_2O_3/GAP binary MGC ingot by machining using a diamond wheel.

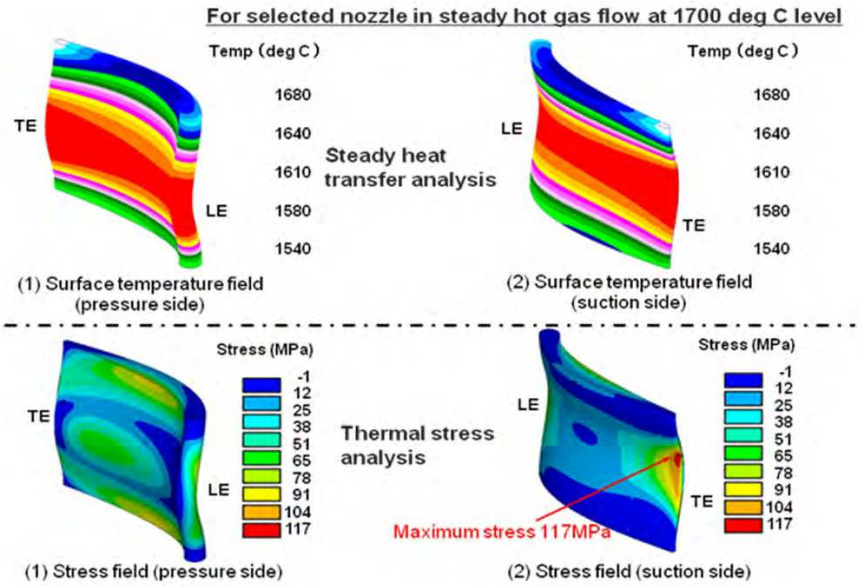

Fig. 17. Steady thermal stress generated during hot gas flow at 1700°C estimated by using numerical analysis.

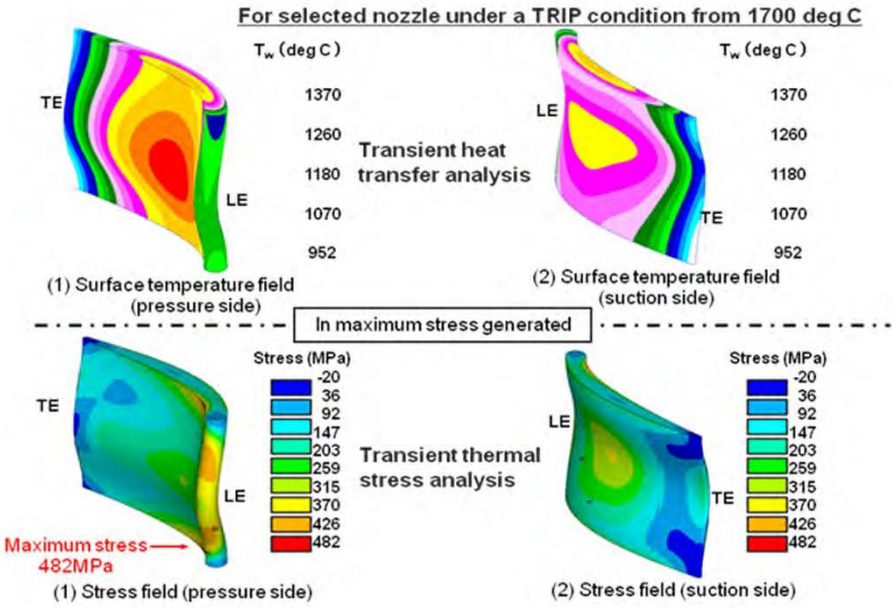

Fig. 18. Transient thermal stress under TRIP condition from 1973 K estimated by using numerical analysis.

7. MGC gas turbine component

Fig.19 shows the SEM images of microstructure of cross-section perpendicular to the solidification direction of the Al_2O_3/YAG and Al_2O_3/GAP binary MGCs after 0 - 1000 hours of heat treatment at 1700 °C in an air atmosphere. In case of Al_2O_3/YAG binary MGC (Fig.19 (a) and (b)) even after 1000 hours of heat treatment, no grain growth of microstructure was observed. While in case of Al_2O_3/GAP binary MGC (Fig. 19 6 (c) and (d)), a slight grain growth was observed. However, both MGCs were shown to be comparatively stable without void formation during lengthy exposure at high temperature of 1973 K in an air atmosphere. This stability resulted from the thermodynamic stability at that temperature of the constituent phases of the single-crystal Al_2O_3, the single-crystal YAG and the single-crystal GAP, and the thermodynamic stability of the interface.

Fig. 20 shows a relationship between flexural strength at room temperature and the time of heat treatment at 1973 K in an air atmosphere. The Al_2O_3/YAG binary MGC has about 300 – 370 MPa of the flexural strengths after the heat treatment for 1000 hours at 1973 K in an air atmosphere. This strength is the same value as the as-received. While, the flexural strength of the Al_2O_3/GAP binary MGC after heat treatment for 1000 hours at 1973 K in an air atmosphere has about 500 MPa slightly lower than that of the as-received. In the case of the Al_2O_3/GAP binary MGC, although the a little drop in the flexural strength in seen a shot time later of the heat treatment, the flexural strength after 200 hours of the heat treatment is independent of the heat treatment time. Both MGCs exhibited good thermal stability at very high temperature of 1973 K in an air atmosphere.

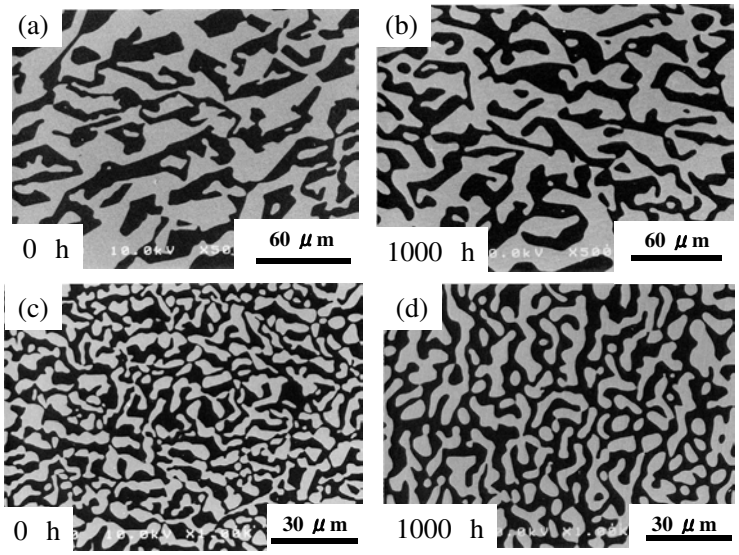

Fig. 19. SEM images showing microstructural changes of cross-section perpendicular to the solidification direction of binary MGCs before and after heat treatment until 1000 hours at 1973 K in an air atmosphere. (a) and (b): the Al_2O_3/YAG binary MGC. (c) and (d): the Al_2O_3/GAP binary MGC. (a) and (c) are for 0 hour. (b) and (d) are for 1000 hours.

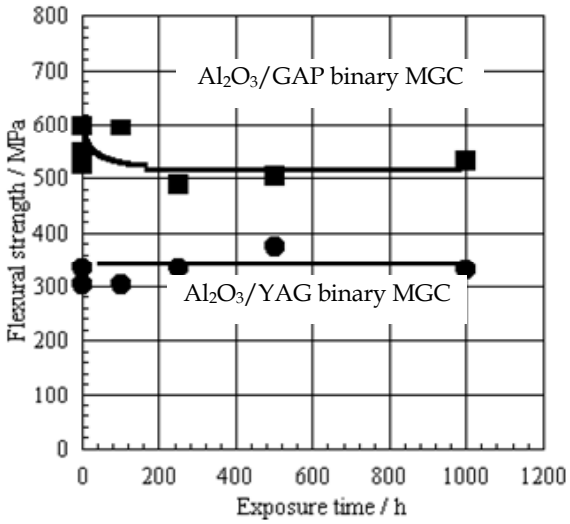

Fig. 20. Relationship between flexural strength at room temperature and time of heat treatment at 1973 K in an air atmosphere.

8. New Bridgman type furnace

MGCs are fabricated by unidirectional solidification from molten oxide eutectic compositions. The melting experiments are conducted at very high temperatures, hence a new Bridgman-type furnace, designed to accurately control many process parameters at super high temperatures, was acquired. Fig.21 is the schematic drawing of the new Bridgman-type furnace. The equipment consists of a casting chamber, a vacuum chamber and a driving device. The schematic on the right of Fig. 21 shows the casting chamber. The casting chamber consists of a heating and melting zone and a cooling zone. Both zones can independently control their temperatures by high frequency induction heating. The Bridgman type furnace has the following features: (1) measurement and control of high temperature around 2300 K, (2) precise control of temperature gradients at near the liquid-solid interface by controlling the melting zone and the cooling zone independently, and (3) the ability to fabricate large MGC components with a maximum size of 300 mm in diameter and 500 mm in length.

Fig.22 shows the external appearance of the new Bridgman-type furnace at JUTEM (Japan Ultra-High Temperature Materials Research Center). The equipment consists of a controller panel, a cooling water system, a casting chamber and a vacuum pump system. The upper right figure is the main controller panel. The lower right figure shows the inside of the casting chamber. The casting chamber consists of a heating and melting zone and a cooling zone. The heating and melting zone is used to heat a Mo crucible and then melt an oxide eutectic raw material in the Mo crucible. The cooling zone is used to control the temperature gradient close to an interface between solid and liquid. Both zones can independently control their temperatures by high frequency induction heating. The lower left figure shows the cooling water equipment.

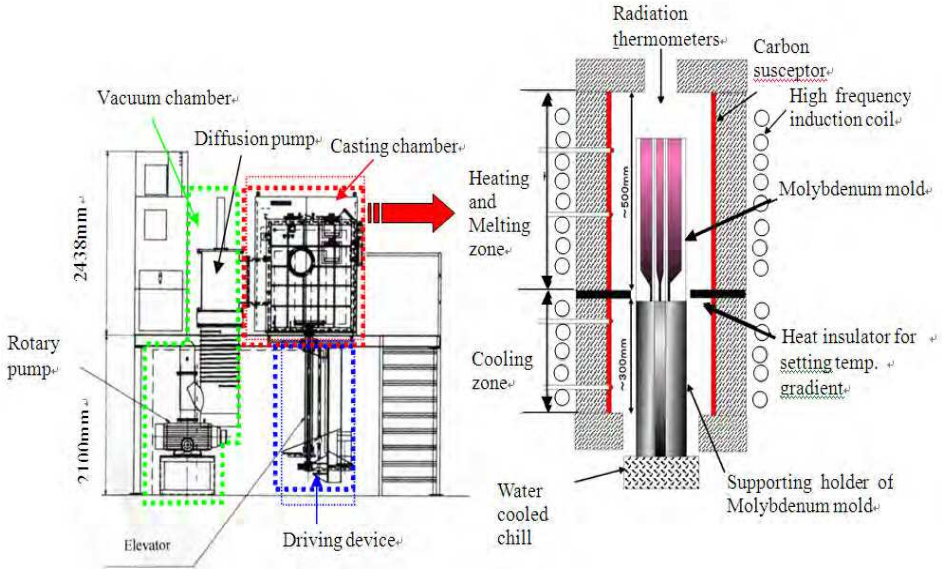

Fig. 21. Schematic drawing of new Bridgman-type furnace

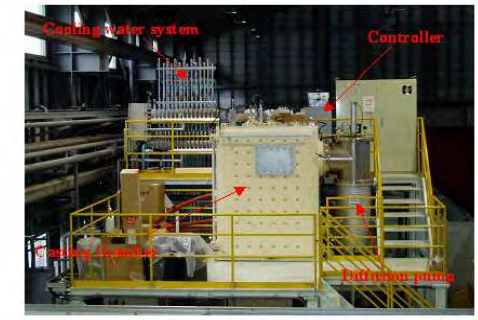

External appearance of new Bridgman-type furnace at JUTEM

Main controller panel

Cooling water equipment

Inside of casting chamber

Fig. 22. New Bridgman-type furnace

9. Molybdenum crucible for near-net shape casting

9.1 Plasma sprayed molybdenum mold

Molybdenum is the most suitable material for fabricating MGC parts. Fabrication of a near-net-shaped crucible was attempted by plasma spraying of molybdenum powder on a copper model with a complex shape. The mold was obtained by plasma spraying the molybdenum powders on the copper model. Fig.23 shows plasma spraying of the molybdenum crucible for near-net-shape casting. The plasma spraying was performed using Mo powder with a particle diameter of 20~40 μm in a vacuum atmosphere (about 100 mmHg). The copper model was completely removed from the plasma sprayed mold by melting at 1473 K. Fig.24 shows the external appearance of the plasma sprayed molybdenum mold and its cross section at the middle of the longitudinal direction. The microstructure of the plasma sprayed Mo mold is relatively homogeneous, though it does include some pores. The thickness of wall of the mold is 2-3 mm.

Fig.25 shows the roughness of the internal surface of the plasma sprayed molybdenum mold, with or without shot peening to the Cu model, together with the relatively smooth surface of an extruded molybdenum mold for comparison. Shot peening causes the internal surface of the Cu model to be very rough. It is difficult to remove the MGC from the molybdenum mold after unidirectional solidification. Hence, it is necessary to improve the surface roughness of the mold. To achieve this, the molybdenum powder was plasmasprayed without shot peening to the Cu model. To improve the adhesion of the molybdenum powder, the temperature of the copper model was raised by about 150 K

compared to the plasma spraying with shot peening. The surface roughness of the internal wall of the plasma sprayed mold without shot peening to the Cu model was found to be significantly improved compared with that of the plasma sprayed mold with shot peening. The surface roughness of the plasma sprayed molybdenum mold without shot peening to the Cu model appears to be comparable to that of the extruded molybdenum mold.

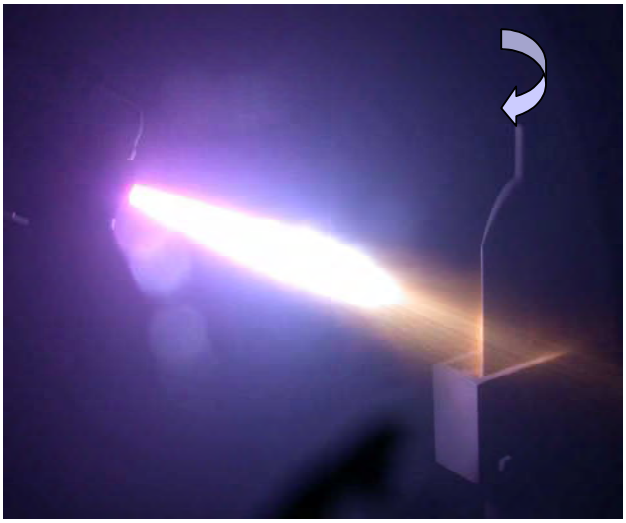

Fig. 23. A plasma spraying scene to produce the quasi-turbine nozzle mold for near-net shaped casting.

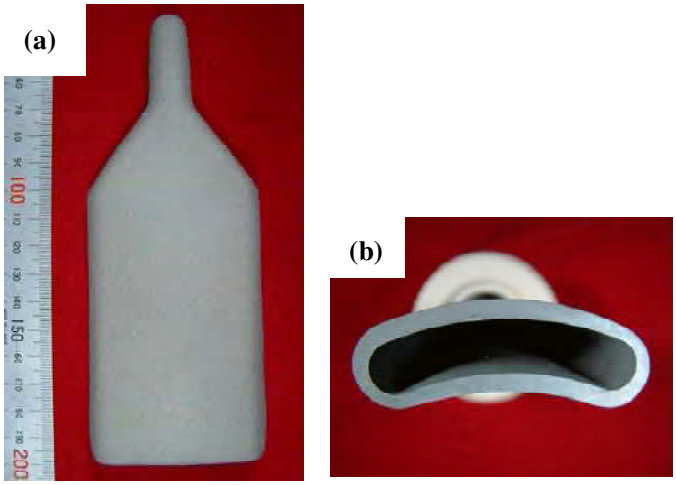

Fig. 24. Plasma sprayed crucibles. (a) External appearance of the crucible manufactured by plasma spraying of molybdenum powder on the copper master mold and (b) its cross-sectional diagram.

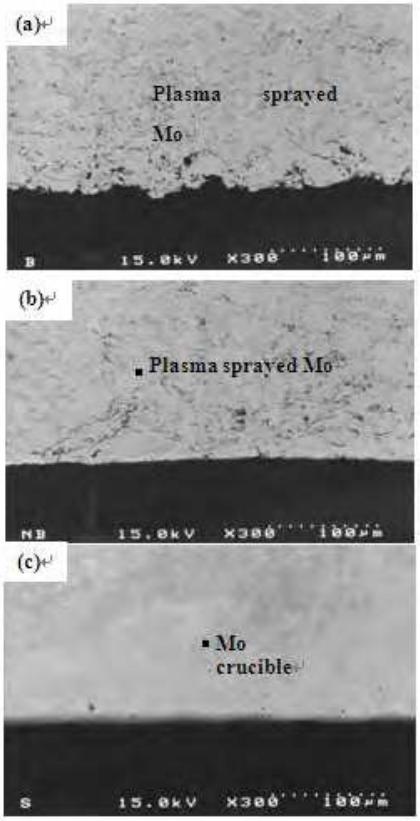

Fig. 25. Cross-sectional microstructure showing roughness on the internal surface of plasma sprayed crucible by Mo powder (a) with shot peening, (b) without shot peening, and (c) Mo crucible produced by extrusion.

9.2 Unidirectional solidification

Fig. 26 shows SEM images of the microstructure of a cross-section perpendicular to the solidification direction of an Al_2O_3/YAG and an Al_2O_3/GAP binary MGC fabricated using the plasma sprayed molybdenum mold and the new Bridgman type furnace. For the Al_2O_3/YAG binary MGC (Fig. 26 (a)), the light area is the YAG phase with a garnet structure, and the dark area is Al_2O_3 phase with a hexagonal structure in the same way as The dimensions of the microstructures are 15-20 μm, smaller than that of the Al_2O_3/YAG binary MGC produced using the extruded mold. Homogeneous microstructures with no pores or colonies are observed in the Al_2O_3/YAG binary MGC fabricated using the plasma

sprayed Mo mold. However, the microstructure near the mold is bigger than that for the center.

For the Al_2O_3/GAP binary MGC (Fig. 26 (b)), the light area in the SEM micrograph is the GAP phase, and the dark area is the Al_2O_3 phase in the same way as Fig. 3(b). The dimensions of the microstructures are 2-4 μm, a little smaller than those of the Al_2O_3/GAP binary MGC produced using the extruded Mo crucible. Homogeneous microstructures with no pores or colonies are observed in the Al_2O_3/GAP binary MGC fabricated using the plasma sprayed Mo mold.

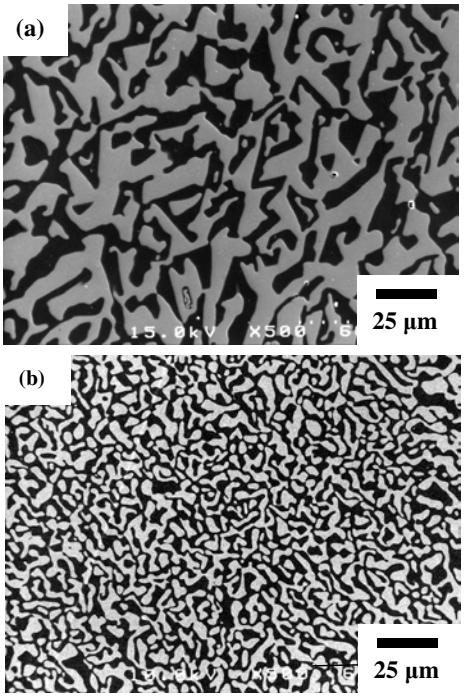

Fig. 26. SEM images of the microstructure of a cross-section perpendicular to the solidification direction of an Al_2O_3/YAG (a) and an Al_2O_3/GAP (b) binary MGC using manufactured using the plasma sprayed Mo mold.

9.3 High temperature strength

Fig. 27 shows the temperature dependence of the flexural strength from room temperature to 1973 K of Al_2O_3/YAG binary MGCs, which was produced by using the plasma, sprayed Mo mold and the extruded Mo crucible. Both MGCs maintain their temperature strength up to 1973 K, with a flexural strength in the range of 260~350 MPa. Namely, the temperature dependence of strength of the Al_2O_3/YAG binary MGC produced using the plasma sprayed Mo mold is almost the same as that of the Al_2O_3/YAG binary MGC produced using the extruded Mo crucible.

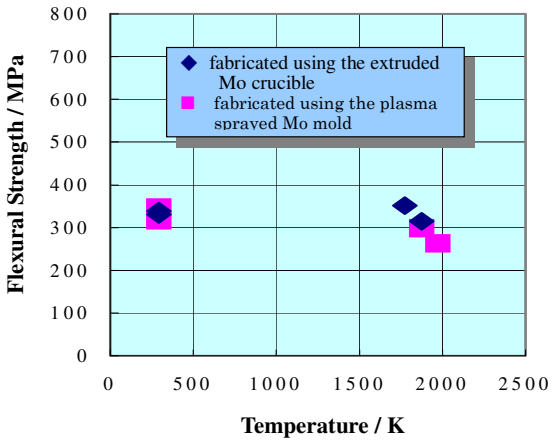

Fig. 27. Temperature dependence of the flexural strength from room temperature to 1973 K of different Al_2O_3/YAG binary MGCs fabricated using the plasma sprayed Mo mold and using the extruded Mo crucible.

10. Conclusions

MGCs have the unique microstructure of a three-dimensionally continuous network of single crystal phases without grain boundaries. Therefore, MGCs have many advantages such as excellent high temperature strength, creep resistance, superior thermal stability as ultra-high temperature structural materials. The NEDO project for a gas turbine system using MGCs has been briefly introduced along with current research topics for system integration and innovative process and manufacturing technology. The manufacturing process of a plasma sprayed molybdenum mold for near-net-shaped casting of the gas turbine component was also introduced. We have recently been successfully fabricated the

Al_2O_3/YAG and Al_2O_3/GAP binary MGCs using plasma sprayed Mo molds and a new Bridgman type furnace. Temperature dependence of strength of the Al_2O_3/YAG binary MGC fabricated using the plasma sprayed Mo mold is almost the same as that of the Al_2O_3/YAG binary MGC produced using the extruded Mo crucible.

11. Acknowledgements

The authors would like to express their thanks to the New Energy and Industrial Technology Development Organization (NEDO) and the Ministry of Economy, Trade and Industry (METI) for the opportunity to conduct "Research and Development of Ultra-high Temperature Heat-resistant Materials MGC".

12. References

Mah, T. & Parthasarathy, T.A. (1990). Processing and mechanical properties of $Al_2O_3/Y_3Al_5O_{12}$(YAG) eutectic composite. *Ceram. Eng. Sci. Proc.,* vol.11, No.9-10, pp. 1617-1627.

Parthasarathy, T.A.; Mah, T. & Matson, L.E. (1990). Creep behavior of an Al_2O_3-$Y_3Al_5O_{12}$ eutectic composite. *Ceram. Eng. Soc. Proc.,* vol.11No.9-10, pp. 1628- 1638.

Parthasarathy, T.A.; Mar, Tai-II & Matson, L.E. (1993). Deformation behavior of an Al_2O_3-$Y_3Al_5O_{12}$ eutectic composite in comparison with sapphire and YA," *J.Am.Ceram. Soc.,* 76[1], pp.29-32.

Stubican, V.S.; Bradt, R.C.; Kennard, F.L.; Minford, W.J. & Sorrel C.C. (1986). Ceramic Eutectic Composites. in *Tailoring Multiphase and Composite Ceramics*, Edited by Tressler, Richard E., Messing, Gary L., Patano, Carlo G. and Newnham Robert E., pp. 103-114.

Waku, Y.; Ohtsubo, H.; Nakagawa, N. & Kohtoku, Y. (1996). Sapphire matrix composites reinforced with single crystal YAG phases. *J. Mater. Sci.,* vol.31, pp. 4663-4670.

Waku, Y.; Nakagawa, N.,; Wakamoto, T.; Ohtsubo, H.; Shimizu, K. & Kohtoku, Y. (1997). A ductile ceramic eutectic composite with high strength at 1873 K. *Nature*, vol.389, pp. 49-52.

Waku, Y.; Nakagawa, N.; Wakamoto, T.; Ohtsubo, H.; Shimizu, K.& Kohtoku, Y. (1998). High-temperature strength and thermal stability of a unidirectionally solidified Al_2O_3/YAG eutectic composite. *J. Mater. Sci.,* vol.33, pp. 1217-1225.

Waku, Y.; Nakagawa, N.; Wakamoto, T.; Ohtsubo, H.; Shimizu, K. & Kohtoku, Y. (1998). The creep and thermal stability characteristics of a unidirectionally solidified Al_2O_3/YAG eutectic composite. *J. Mater. Sci.,* vol.33, pp. 4943-4951.

Waku, Y.; Nakagawa, N.; Ohtsubo, H.; Mitani, A. & Shimizu, K. (2001). Fracture and deformation behaviour of melt growth composites at very high temperatures. *J. Mater. Sci.,* vol.36, pp. 1585-1594.

Courtright, E.L.; Graham, H.C.; Katz, A.P. & Kerans, P.J. (1992). Ultrahigh temperature assessment study – ceramic matrix composites. Materials Directorate, Wright Laboratory, Air Force Materiel Command, Wright-Patterson Air Force Base,1.

Waku, Y.; Sakata, S.; Mitani, A. & Shimizu, K. (2001). A novel oxide composite reinforced with a ductile phase for very high temperature structural materials. *Materials Research Innovations,* vol.5, pp. 94-100.

Waku, Y.; Sakata, S.; Mitani, A.; Shimizu, K. & Hasebe, M. (2002). Temperature dependence of flexural strength of $Al_2O_3/Y_3Al_5O_{12}/ZrO_2$ ternary melt growth composites. *J.Mater. Sci.,* vol.37, No.14, pp.2975-2982.

Yasuda,H.; Ohnaka, I.; Mizutani, Y.; Morikawa, T.; Takeshima, S.; Sugiyama, A.; Waku, Y.; Tsuchiyama, A.; Nakano, T. & Uesugi,K. (2003). unpublished work, Osaka University, Osaka, Japan.

Yasuda,H.; Ohnaka, I.; Mizutani, Y.; Morikawa, T.; Takeshima, S.; Sugiyama, A.; Waku, Y.; Tsuchiyama, A.; Nakano, T. & Uesugi,K. (2005). *Journal of the European Ceramic Society,* vol. 25, pp. 1397-1403.

Frazer, C. S.; Dickey, E.C.; Sayir, A. (2001). *J. Cryst. Growth,* Vol.233, P. 187.

Yoshida, M.; Tanaka, K.; Kubo, T.; Terazone, H. & Tsuruzone, S. (1998). *Proceedings of the international Gas Turbine & Aeroengine Congress & Exibition* (The American Society of Mechanical Engineeers 1998).

Goulette, M. J. (196): *Proceeding of the eighth international symposium on superalloys* (TMS, Pennsylvania 1996).

Y. Waku, Y.; Sakata, S.; Mitani, A.; Shimizu, K.; Ohtsuka, A. & Hasebe, M. (2002). *J. of Mater. Sci.* vol. 37, p. 2975.

Waku, Y. & Sakuma, T. (2000). Dislocation Mechanism of Deformation and Strength of Al_2O_3-YAG Single Crystal Composite at High Temperature above 1700 K. *the Journal of the European Ceramic Society,* vol.20, pp. 1453-1458.

DiCarlo, J. A. & Yun, H. Y. (1999). Thermostructural performance maps for ceramic fibers," in *9th Cimtec World Forum on New Materials Symposium V* – Advanced Structural Fiber composites, Edited by P. Vincenzini, vol.22, pp29-42.

Yun, H.M. and DiCarlo, J.A. (1999). Comparison of the tensile, creep, and rupture strength properties of stoichiometric SiC fibers, *Ceram. Eng. Sci. Proc.,* vol.20, pp. 259-272.

Krause, R.F. Jr.; Luecke, W.E.; French, J.D.; Hockey, B.J. & Wiederhorn, S.M. (1999). Tensile creep and rupture of silicon nitride. *J. Am. Ceram. Soc.,* vol. 82, No.5, pp. 1233-1241.

Ohji, T.; Nakahira, A.; Hirano, T. & Niihara, K. (1994). Tensile creep behavior of alumina/silicon carbide nanocomposite. *J. Am. Ceram. Soc.,* vol.77, No.12, pp. 3259-3262.

Erickson, G.L. (1996). The development and application of CMSX-10. in *Proceedings of the Eighth InternationalSymposium on Superalloys*, September 22-26, 1996, Pennsylvania, USA, Edited by R. D. Kissinger, D. J. Deye, D. L. Anton, A. D. Cetel, M.V. Nathal, T. M.Pollock, and D. A. Woodford., pp.35-44.

Waku, Y.; Nakagawa, N.; Kobayashi, K.; Kinoshita, Y. & Yokoi, S. (2004). Innovative manufacturing Processes of MGC's Components for Ultra High Efficiency Gas Turbine Systems. *ASME TURBO EXPO 2004 – Power for Land, Sea & Air,* 14-17 June 2004, Vienna, Austria.

Nakagawa, N.; Waku,Y.; Wakamoto, T.; Ohtsubo, H., Shimizu, K. & Kohtoku, Y. (1997). The Creep, Oxidation Resistance Characteristics of a Unidirectionally Solidified $Al_2O_3/Er_3Al_5O_{12}$ Eutectic Composite. *6th International Symposium on Ceramic*

Materials & Components for Engines, October 19-24, 1997, Arita, Japan, (1997) pp701-706.

Waku, Y.; Nakagawa, N.; Kobayashi, K Kinoshita, Y. & Yokoi, S. (2003). unpublished work, HPGT Research Association, Tokyo, Japan.

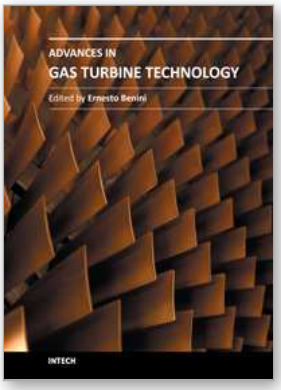

Advances in Gas Turbine Technology

Edited by Dr. Ernesto Benini

ISBN 978-953-307-611-9
Hard cover, 526 pages
Publisher InTech
Published online 04, November, 2011
Published in print edition November, 2011

Gas turbine engines will still represent a key technology in the next 20-year energy scenarios, either in stand-alone applications or in combination with other power generation equipment. This book intends in fact to provide an updated picture as well as a perspective vision of some of the major improvements that characterize the gas turbine technology in different applications, from marine and aircraft propulsion to industrial and stationary power generation. Therefore, the target audience for it involves design, analyst, materials and maintenance engineers. Also manufacturers, researchers and scientists will benefit from the timely and accurate information provided in this volume. The book is organized into five main sections including 21 chapters overall: (I) Aero and Marine Gas Turbines, (II) Gas Turbine Systems, (III) Heat Transfer, (IV) Combustion and (V) Materials and Fabrication.

INTECH
open science | open minds

InTech Europe
University Campus STeP Ri
Slavka Krautzeka 83/A
51000 Rijeka, Croatia
Phone: +385 (51) 770 447
Fax: +385 (51) 686 166
www.intechopen.com

InTech China
Unit 405, Office Block, Hotel Equatorial Shanghai
No.65, Yan An Road (West), Shanghai, 200040, China
中国上海市延安西路65号上海国际贵都大饭店办公楼405单元
Phone: +86-21-62489820
Fax: +86-21-62489821